Structural investigation of carbon morphology on Ni/cerium-zirconium oxide catalysts used for the biogas dry reforming reaction

Ioannis Tsiaoussis[1*], Nikos D. Charisiou[2], Maria A. Goula[2], Lazaros Tzounis[3], George Vourlias[1], Ioannis V. Yentekakis[4], Remi Chassagnon[5], Valerie Potin[5], Bruno Domenichini[5]

[1]*Physics Department, Aristotle University Thessaloniki, Thessaloniki 54124, Greece*

[2]*Laboratory of Alternative Fuels and Environmental Catalysis, Department of Environmental and Pollution Control Engineering, Western Macedonia University of Applied Sciences, Koila, Kozani, 50100, Greece*

[3]*Composite and Smart Materials Laboratory (CSML), Department of Materials Science & Engineering, University of Ioannina, Ioannina 45110, Greece*

[4]*School of Environmental Engineering, Technical University of Crete, Chania 73100, Greece*

[5]*ICB, UMR 6303 CNRS-Université de Bourgogne Franche-Comté, BP 47870, Dijon F-21078, France*

[*]Corresponding author; Tel: (+30) 2310998168 Office: (+30) 2310998146 Lab; E-mail: tsiaous@auth.gr

Received: 10 August 2017, Revised: 15 August 2017 and Accepted: 06 September 2017

DOI: 10.5185/amp.2017/921
www.vbripress.com/amp

Abstract

In the present work, we investigated the structural morphology of carbon species deposited on nickel catalysts supported on CeO_2-ZrO_2 (18.8 wt.% ceria), prepared by wet impregnation, during the dry reforming of methane (DRM) reaction by using Thermo-gravimetric Analysis (TGA), Raman Spectroscopy, X-ray diffraction (XRD), High Resolution Transmission Electron Microscopy (HRTEM) and Scanning Transmission Electron Microscopy- Energy dispersive spectroscopy (STEM-EDS). TGA results show that the amount of deposited carbon decreases upon increasing reaction temperature, which is consistent with the thermodynamics of the reactions responsible for carbon formation, and Raman analysis points to a simultaneous increase in its graphitization degree. XRD measurements reveal the existence of 2H-Graphite and TEM imaging mode as well as SAED patterns depict that in all temperatures under which the catalysts were tested (550, 650, 750 and 800 ^oC), the formation of multi wall carbon nanotubes (MWCNT). HRTEM observations also reveal that the Ni nanoparticles are often enclosed by the MWCNT. HRTEM images identify nanocrystalline areas with a tetragonal phase, P42/nmc(137), of $Ce_{1-x}Zr_xO_2$, and STEM-EDS analysis at the nanometer scale confirms a correlation between Ce and Zr in the average atomic ratio (%), 1 to 5.19 - 6.94 respectively. The results presented herein confirm that biogas mixtures can be used as precursors for the production of MWCNTs.

Keywords: Biogas, dry reforming of methane, HRTEM, multi wall carbon nanotubes, Ni catalysts, ceria-zirconia supports.

Introduction

Carbon nanotubes (CNTs) were discovered more than a quarter of a century ago by Iijima [1] and are considered as a major breakthrough in nanotechnology development. This is due to their outstanding electronic, thermal, adsorption and mechanical properties, which mean that CNTs can be used in a wide range of applications [2, 3]. CNTs are divided into single wall (SWCNTs, 0.4-2 nm in diameter) and multi wall (MWCNTs, 2-100 nm in diameter), based on the number of walls comprising their structure [4]. MWCNTs are attracting attention as they have the potential to be used as chemical sensors, field emitters and electrode catalytic supports [5]. MWCNTs can be produced from organic precursors such as methane [6], glycerol [7], ethanol [8] or other hydrocarbon sources using techniques such as epitaxial growth [9] and chemical vapor deposition (CVD) [10]. CVD is a catalyst assisted process that takes place at temperatures ranging from 300-1200^oC. The catalysts that are used are usually transition metals, such as Ni, Fe or Co supported on a variety of substrates [11].

Another catalytic process that is of extreme interest is the dry reforming of biogas (DRB), as it allows the conversion of CH_4 and CO_2 (i.e., the principal greenhouse gases) into syngas, which is a building block for the synthesis of oxygenated chemicals and hydrocarbons from Fisher – Tropsch synthesis [12, 13]. However, a condition that needs to be met for the use of DRB in industrial applications is the development of cheap, highly active and

stable catalysts [14, 15]. It is noted that the DRB is a highly endothermic reaction (ΔH^{o}_{298}=+247 kJ/mol), which is influenced by the simultaneous occurrence of a number of reactions, amongst which some that favor carbon deposition [16, 17]. Although Ni catalysts are both relatively cheap and offer exceptional activity, they suffer from deactivation due to carbon formation and metal particles sintering due to a lack of adequate thermal stability [18,19]. Interestingly, a number of works have reported on the formation of carbon nanofibers (CNFs) or CNTs during the biogas dry reforming reaction. Gurav et al. [20] tested Ni catalysts supported on Gd doped with ceria and examined the nature of coke using TEM and Raman spectroscopy. They identified CNTs with an I_D/I_G ratio close to 1.0. Titus et al. [21] while testing NiO–MgO–ZrO_2 catalysts identified MWCNT of varying diameters using TEM. Similarly, Serrano-Lotina and Daza [22], using TEM, reported the formation of MWCNTs on a La-Ni/MgAlO catalyst. Arguably, the development of catalysts that will be highly active and stable for the DRB (thus, suitable for syngas production), which will also produce carbon nanotubes, is a major research challenge that has the potential to offer extra added value on the process and affect the economics of the reaction. In fact, very few studies, if any, have focused on the use of biogas as a precursor for the production of CNTs.

In a previous work [23], we examined the DRM catalytic efficiency of Ni dispersed on three commercially available catalytic supports (ZrO_2, La_2O_3-ZrO_2 and CeO_2-ZrO_2) for a methane rich CH_4/CO_2 mixture (with a ratio equal to 1.5) that was diluted by 50% in He. We found that the modification of the zirconia support by either ceria or lanthana produces catalysts that are significantly more efficient and durable in comparison to the unmodified catalyst. Moreover, we reported that on the spent catalysts, carbon with filamentous tube-like morphology was formed with the SAED patterns revealing the formation of characteristic graphitic structures (due to the multi-wall tubes).

Prompted from the above, we further expanded our studies on the Ni/$Ce_{1-x}Zr_xO_2$ catalyst, using undiluted CH_4/CO_2 mixtures, in order to help inducing the formation of carbon with the purpose of studying its characteristics as a function of the applied conditions. To this purpose, we have conducted a number of stability tests at different reaction temperatures and used X-ray diffraction (XRD), thermogravimetric analysis (TGA), Raman spectroscopy, High Resolution Transmission Electron Microscopy (HRTEM) and Scanning Transmission Electron Microscopy combined with energy-dispersive X-ray spectroscopy (STEM- EDS) were used to characterize the coke deposited on the spent catalyst samples, as well as, to obtain local and precise chemical analysis at the nanometer scale.

Experimental

Catalyst preparation

The catalysts were prepared via the wet impregnation of a commercially available (Saint Gobain NorPro) CeO_2-ZrO_2 support (18.83 wt. % of Ceria) in a $Ni(NO_3)_2 6H_2O$ (Sigma Aldrich) aqueous solution of appropriate concentration in order to obtain catalysts with a Ni loading of about 8 wt. %. Water was evaporated from the slurries under continuous stirring at 75 ^{o}C for 5 h. The suspensions were then dried at 120 ^{o}C for 12 h and calcined in air at 800 ^{o}C for 4 h.

Catalyst characterization

Thermogravimetric analysis

The amount of carbon deposited on the spent catalysts, as well as its thermal decomposition process was obtained using a thermogravimetric analyzer (TGA), on a Leco TGA701 instrument; the procedure followed has been described in detail in [24].

Raman spectroscopy

Raman spectroscopy was also used to investigate the coke deposited on the spent catalytic samples. For this purpose, a WITEC alpha 300R (Germany) micro-Raman system was used. The instrument is equiped with a 20× long distance objective (0.35 numerical aperture) in the back-scattering geometry with an excitation wavelength of 532 nm from an Ar+ ion laser. The laser power was set at 2 mW and was calibrated against a silicon standard. For each sample, at least three Raman spectra were collected in different areas to assess the homogeneity of the investigated material. All spectra collected from the same samples showed similar features confirming the homogeneity of the carbon deposits.

X-ray diffraction (XRD)

The crystal structures were identified by X-ray Diffractometry (XRD) using a water-cooled Rigaku Ultima+ diffractometer with Cu Ka radiation (λ=1.5406 Å), a step size of 0.05◦ and a step time of 3 s, operating at 40 kV and 30 mA.

The lattice parameters were calculated with the "Jade" software from peak location and miller indices. The average particle size (*D*) was estimated according to the Scherrer equation [25]:

$$D = 0.90\lambda/\beta cos\theta$$

Where, θ *is* the diffraction angle of the (111) peak of the cubic phase or the (101) peak of the tetragonal phase and β is the full width at half-maximum (fwhm) of the (111) or the (101) peak (in radian), which is calibrated from high purity silicon.

HRTEM

The structure for all spent samples was characterized by high resolution transmission electron microscopy (HRTEM), with a TEM JEOL 2100 FEG operating at 200 kV. The elemental chemical composition was determined by energy-dispersive X-ray spectroscopy (EDX) with a Bruker Quantax XFlash 5030T SDD in scanning mode

(scanning probe of 2 nm). The scanning technique of TEM (STEM) was used to get local and precise chemical analysis at the nanometer scale. We have used for the quantification process a Bruker AXS Microanalysis System. The samples were dispersed in a methanol solution using an ultrasonic bath; a small drop, of the methanol suspension containing uniformly dispersed oxide powders, was taken and deposited on carbon-coated copper grids, and dried at 20 ºC.

Catalytic testing

The catalytic tests were performed at atmospheric pressure, using a continuous flow fixed bed tubular reactor. The gas mixture used as feed in the reactor inlet consisted of 55% CH_4, 35% CO_2 and 10% Ar, corresponding to a CH_4 /CO_2 molar ratio equal to 1.56, simulating a typical biogas mixture. The catalyst pre-condition procedure involved the in situ catalyst reduction under hydrogen flow (100 mL min^{-1}) at 800ºC for 1 h. Then the reactor was returned to the temperature of interest under He flow (100 mL min^{-1}). Short, constant time-on-stream tests (of 10 h) were performed at a constant Weight Hour Space Velocity (WHSV, equal to 40,000 mL g^{-1} h^{-1}) at four different temperatures, namely 550ºC, 650ºC, 750ºC and 800ºC. Note that a fresh catalytic sample was used at the beginning of every experiment.

Results and discussion

Thermogravimetric analysis

The amount of coke deposited on to the spent catalysts tested at the different temperatures has been measured by TGA and the results are depicted in **Table 1**. It is clear that the amount decreases with an increase in the reaction temperature. This is consistent with the thermodynamics of the reactions that are responsible for carbon formation [26].

Table 1. Quantity of carbon formed on the spent catalytic samples as measured by TGA.

	Carbon, % (100-Weight Loss)			
Temperature	550ºC	650ºC	750ºC	800ºC
$Ni/Ce_{1-x}Zr_xO_2$	70.2	48.3	41.0	18.9

Moreover, from **Fig. 1** (differential thermogravimetry – DTG), it is obvious that the main oxidation process takes place between 500-700ºC, which indicates the presence of graphitic carbon allotropes, such as CNTs [27, 28]. In addition, **Fig.1** shows that the rate of oxidation is decreasing with the increase of the reaction temperature, which indicates that the carbon formed becomes more crystalline, in accordance with the Raman findings presented below.

Raman spectroscopy

The Raman spectra of all spent catalysts are presented in **Fig. 2** and in all cases two characteristic peaks located at around 1344 cm^{-1} (D-band) and 1580 cm^{-1} (G-band) can be observed. The D-band is associated with the disordered structural form of crystalline carbon species, while the G-band is associated with graphitic carbon with high degree of crystallinity, order and symmetry [29]. The degree of crystallinity of the carbon formed during the reaction can be gauged by the relative intensity of the D and G bands (I_D/I_G). More specific smaller values indicate higher crystallinity due to higher contribution of the graphitized carbon. From **Fig. 2**, it is clear that the degree of crystallinity increases with an increase of the reaction temperature (1.44, 0.99, 0.71 and 0.68) at 550ºC, 650ºC, 750ºC and 800ºC, respectively. Moreover, the absence of Radial Breathing Modes (RBM) at 100-300 cm^{-1} indicates that the CNT are of multiwall type [30], in agreement with the TEM findings presented below.

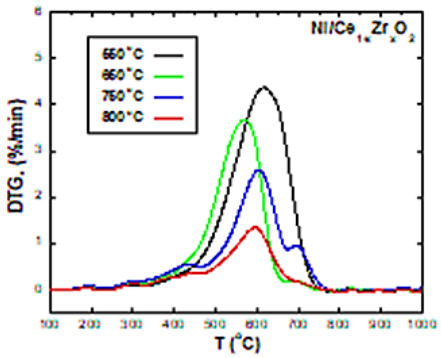

Fig. 1. Rate of carbon oxidation of the $Ni/Ce_{1-x}Zr_xO_2$ catalyst at the four different temperatures the reaction took place.

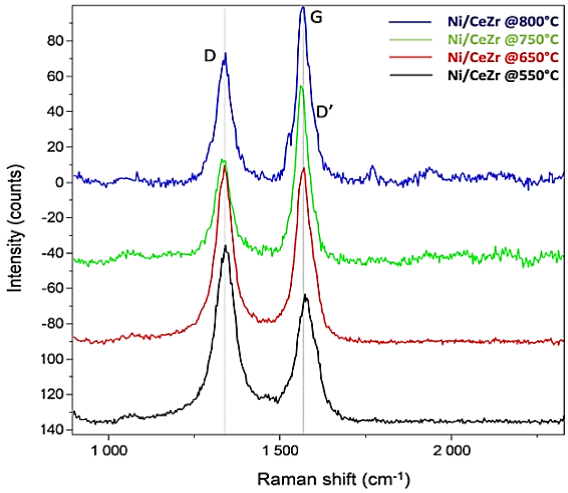

Fig. 2. Raman spectra of the $Ni/Ce_{1-x}Zr_xO_2$ catalyst at the four different temperatures the reaction took place.

Structural characterization of catalysts

X-ray diffraction (XRD)

The XRD patterns of the spent catalytic samples are presented in, **Fig. 3**. For all temperatures, the first diffraction peak is observed at the 2θ between 26.16º - 29.38º corresponding to the reflection of the (002) planes of the hexagonal phase 2H-Graphite (PDF#41-1487).

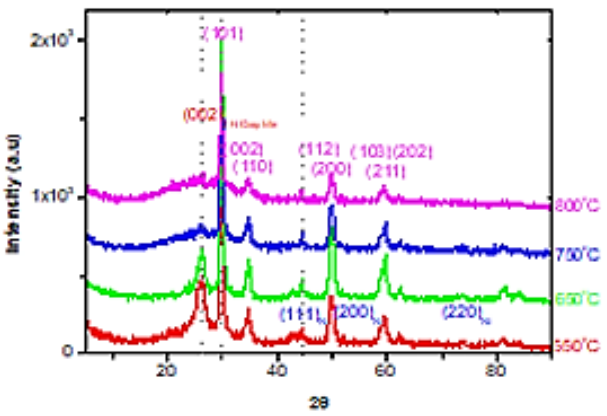

Fig. 3. XRD patterns of the catalytic samples at different temperatures, where the planes of the hexagonal phase 2H-Graphite, the main Ni reflection peaks, and the planes of the tetragonal phase $Ce_{0.16}Zr_{0.84}O_2$ are displayed.

The slight peak shift and the width variation observed, as the samples were tested at increased temperatures, are indications that the crystallinity of the 2H-Graphite increases [31]. This is consistent with the Raman findings presented below. Additional peaks of 2H-Graphite can be identified at the 2θ angles 42.22º, 44.39º, 54.54º, corresponding to the (100), (101) and (004) planes respectively.

Ni reflection peaks can be identified at the 2θ angles 44.50º, 51.84º, and 76.37º they correspond to the (111), (200) and (220) planes of the cubic nickel phase (PDF#04-0850). It is observed that the intensity value of metallic nickel remains unaffected by the reaction temperature.

The absence of Bragg diffraction peaks of pure CeO_2 associated with the absence of ZrO_2 diffraction peaks, suggests the formation of a complex solid $Ce_{1-x}Zr_xO_2$, as previously reported [23]. The tetragonal phase of $Ce_{0.16}Zr_{0.84}O_2$ is identified with the main peak of the planes (101) at the 29.87º (PDF#38-1437). Additionally, to the main peak, reflections of the (002), (110), (112), (200), (103), (211) and (202) planes are visible with the corresponding 2θ angles at 34.12º, 34.82º, 49.60º, 50.10º, 58.50º, 59.35º and 62.05º. As far as the atomic ratio x of Zr, by the formation of a complex solid $Ce_{1-x}Zr_xO_2$ takes the value 0.8, a stable tetragonal phase is presented as previously reported by Rui Si at al. [32].

The lattice constants of the tetragonal phase $Ce_{0.16}Zr_{0.84}O_2$ were calculated using the "Jade" software, and the results are presented in the table below.

Table 2. Calculation of the lattice parameters of the tetragonal phase $Ce_{0.16}Zr_{0.84}O_2$.

	Lattice Constants		
t-phase $Ce_{0.16}Zr_{0.84}O_2$	a	B	c
calculated values	3.6341Å	3.6341Å	5.2445Å
theoretical values	3.627Å	3.627Å	5.2336Å
cubic phase Ni	a	B	c
calculated values	3.5146Å	3.5146Å	3.5146Å
theoretical values	3.5238Å	3.5238Å	3.5238Å

The average grain size for the nanocrystalline particles with t-phase, space group P42/nmc(137) was estimated, using the Scherrer equation and was found between 18 and 25nm.

HRTEM studies

Selected area electron diffraction patterns (SAED) have been taken on different areas of the catalysts. A typical SAED patterns revealed the existence of three different phases for both temperatures (550ºC, 800ºC). The hexagonal phase of the 2H-Graphite, Space Group P63/mmc (164), the cubic phase of Nickel, SG Fm3m (225), and the tetragonal phase, SG P42/nmc(137), $Zr_{0.84}Ce_{0.16}O_2$ were identified. The results are in a good agreement with the XRD pattern analysis.

Low magnification micrographs show in one case Fig.4a at a specific point a small number of MWCNTs 2H-Graphite. On the other side at 800ºC in **Fig. 4b,** a characteristic morphology of the deposited carbon in form of MWCNTs, quite dense, is observed.

Further investigations have shown that, the amount of the deposited carbon decreases upon increasing reaction temperature which is consistent with the thermodynamics of the reactions responsible for carbon formation, as it is detected in the TGA results.

Moreover, low magnification micrographs show a good dispersion for the metallic Ni nanoparticles (dark particles in **Fig. 4**), identified also in dark field images by STEM-EDS below.

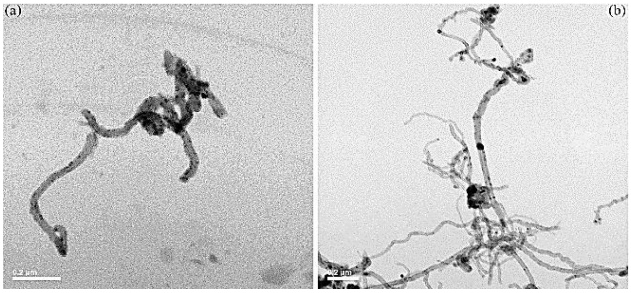

Fig. 4. Low magnification micrographs show in one case Fig.4a at a specific point a small number of MWCNTs 2H-Graphite, a characteristic morphology of the deposited carbon in form of MWCNTs, quite dense, is observed in Fig.4b.

In some other areas, an aggregation of nanoparticles is predominating. SAED pattern analysis, as well as HRTEM investigations in those areas show the existence of the tetragonal phase of $Ce_{0.16}Zr_{0.84}O_2$ as it is exhibited in **(Fig. 5c, d).** On the upper part of the high-resolution micrograph of **Fig. 5a, b,** Nickel nanoparticles are presented enclosed in MWCNTs. Fast Fourier Transformations (FFTs) on those areas show the characteristic pattern of the cubic phase for metallic Nickel, with the zone axis B=[110] in (a) and the indication of the (111) planes and (002) planes of 2H-Graphite in (b). At the bottom of HRTEM micrographs in Fig.5c, d crystalline areas are presented with the t-phase of $Ce_{0.16}Zr_{0.84}O_2$. FFTs have been taken to measure the exact experimental values in d-spacings. A typical FFT

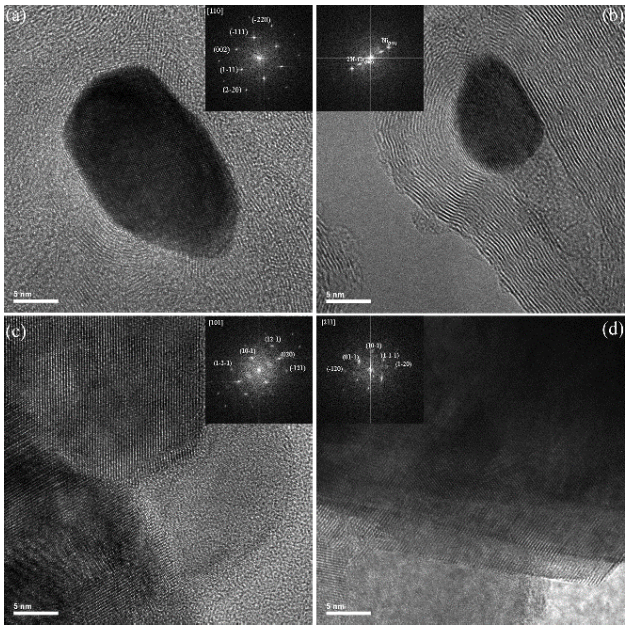

Fig. 5 HRTEM micrographs of Nickel nanoparticles enclosed in MWCNTs are presented in **Fig. 5a**, **b**. FFTs on those areas show the characteristic pattern of the cubic phase for metallic Nickel, with the zone axis B= [110] in (Fig.5a) and the indication of the (111) planes and (002) planes of 2H-Graphite in (Fig.5b). At the bottom of HRTEM micrographs in **Fig. 5c, d** crystalline areas with the t-phase of $Ce_{0.16}Zr_{0.84}O_2$ are presented. FFT patterns as inset, with the zone axis B= [101] and [211] are displayed in (c) and (d) respectively.

pattern is displayed as inset in (c) at 550ºC with the zone axis B= [101] and the experimental values have been measured and found to be 0.258nm, 0.212nm and 0.124nm for the planes (110) (102) and (104), very close to the theoretical ones. In the other case (d) at 800ºC, the FFT pattern show a zone axis B= [211] of the t-phase.

STEM EDS analysis

High-angle annular dark-field scanning transmission electron microscopy (HAADF-STEM) images have been taken in order to exhibit the metallic Ni nanoparticle dispersion in the support catalyst matrix, to display the MWCNTs and to present areas with an aggregation of nanocrystallites, which is the exact point, to find out the tetragonal phase of $Ce_{0.16}Zr_{0.84}O_2$. STEM micrographs in **(Fig. 6 a, b),** show in general a homogeneous distribution of the Ni nanoparticles, with a size in the range of 20-25nm. Many of them, as previously mentioned in the discussion of the HRTEM micrographs, are encapsulated by the MWCNTs formed. On the other hand, STEM-EDS spectra **(Fig. 6 c, d)** at different positions, have been taken in order to perform a more precise chemical analysis at the nanometer scale. The quantification results for both cases are similar, and they show that the correlation in the average atomic ratio (%) between Cerium and Zirconium, varies between 1to 5.19 - 6.94 respectively. This is an evidence that the t-phase P42/nmc(137) of $Ce_{0.16}Zr_{0.84}O_2$ is present.

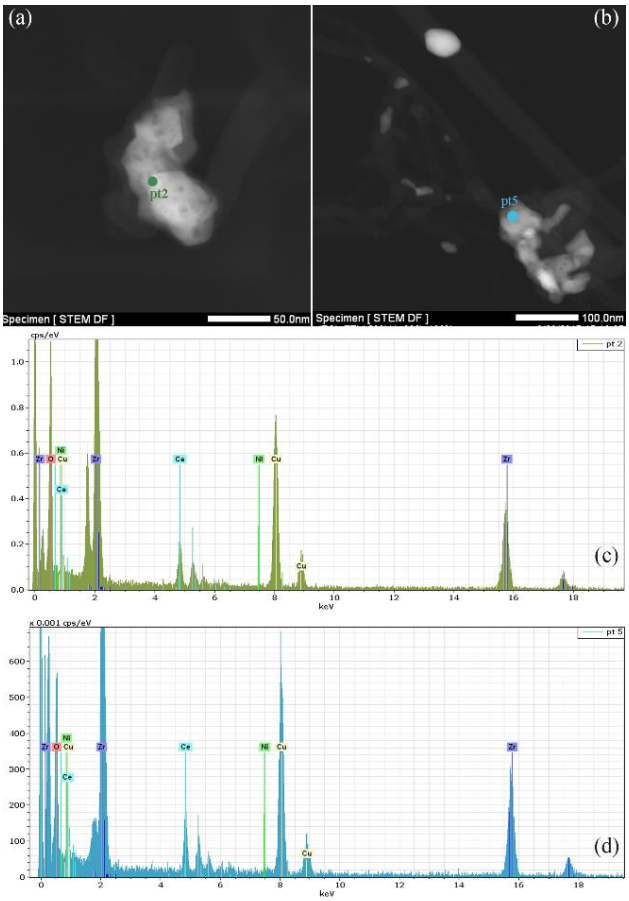

Fig. 6 STEM micrographs in (Fig.6 a,b), show a homogeneous distribution of the Ni nanoparticles, with a size in the range of 20-25nm. STEM-EDS spectra (Fig.6 c,d) at different positions, have been taken in order to perform a more precise chemical analysis. Quantification results for both cases are similar, and they show that the correlation in the average atomic ratio (%) between Ce and Zr varies between 1to 5.19 - 6.94 respectively.

Conclusion

A $Ni/Ce_{1-x}Zr_xO_2$ catalyst was prepared by wet impregnation technique and tested for the biogas dry reforming reaction. The experiments were undertaken at different temperatures and were designed with the purpose of investigating the structure and morphology of the carbon formed. TGA results have shown that the amount of deposited carbon decreases as the reaction temperature increases from 550ºC to 800ºC. This is simultaneously accompanied by an increase in the graphitization degree, as confirmed by Raman spectroscopy. Three different phases are present in all the reaction temperatures, confirmed by XRD data and HRTEM measurements; multi wall carbon nanotubes (MWCNTs) with the h- phase of 2H-Graphite, the c- phase of Ni, and the t-phase of $Ce_{0.16}Zr_{0.84}O_2$. Furthermore, STEM-EDS spectra quantified the relationship in the average atomic ratio (%) between Cerium and Zirconium and confirm, with great certainty the existence of the t-phase P42/nmc(137) of $Ce_{0.16}Zr_{0.84}O_2$. The work presented herein confirms that biogas mixtures can be used as precursors for the production of MWCNTs.

Acknowledgements

N.C. and M.G. are grateful for financial support provided by the Committee of the Special Account for Research Funds of the Western Macedonia University of Applied Sciences (ELKE/ TEIWM Grant number: 80126). L. T gratefully acknowledges the Bodossaki Foundation for financial support.

I.T. would like to thank Prof. Bruno Domenichini for the access to the Jeol 2100 FEG (200kV) at the University de Bourgogne.

Author's contributions

I.T, N.C, conceived and planned the experiments. I.T, G.V, L.T, N.C, R.C performed the experiments. I.T, L.T, N.C, M.G, I.V.Y, R.C, V.P contributed to the interpretation of the results. I.T, N.C, R.C, V.P, B.D wrote the paper. All authors discussed the results and contributed to the final manuscript. Authors have no competing financial interests.

Supporting information

Supporting informations are available from VBRI Press.

References

1. Iijima, S.; *Nature*, **1991**, *354*, 56. **DOI:** 10.1038/354056a0
2. Adamska, M.; Narkiewics, U.; *J Fluor Chem*, **2017**, *200*, 179. **DOI:** 10.1016/j.jfluchem.2017.06.018
3. Song, X.; Shang, S.; Chen, D.; Gu, X.; *Constr Build Mater*, **2017**, *133*, 57. **DOI:** 10.1016/j.conbuildmat.2016.12.034
4. De Volder, M.F.L.; Tawfick, S.H.; Baughman, R.H.; Hart, A.J.; *Science*, **2013**, *339*, 535. **DOI:** 10.1126/science.1222453
5. Kim, W.G.; Yong, S.D.; Yook S.J.; Ji, J.H.; Kim, K.H.; Bae, G.N.; Chung, E.K.; Kim, J.H.; *Carbon*, **2017**, *122*, 228. **DOI:** 10.1016/j.carbon.2017.06.050
6. Allen, M.J.; Tung, V.C.; Kaner, R.B.; *Chem Rev*, **2010**, *110*, 132. **DOI:** 10.1021/cr900070d
7. Velasquez, M.; Batiot-Dupeyrat, C.; Gallego, J.; Santamaria, A.; *Diam Relat Mater*, **2014**, *50*, 38. **DOI:** 10.1016/j.diamond.2014.08.015
8. Gallego, J.; Sierra, G.; Mondragon, F.; Barrault, J.; Batiot-Dupeyrat C.; *Appl Catal A Gen*, **2011**, *397*, 73. **DOI:** 10.1016/j.apcata.2011.02.017
9. Berger, C.; Song, Z.; Li, X.; Wu, X.; Brown, N.; Naud, C.; Mayou, D.; Li, T.; Hass, J.; Marchenkov, A.N.; *Science*, **2006**, *312*, 1191. **DOI:** 10.1126/science.1125925
10. Kim, K.S.; Zhao, Y.; Jang, H.; Lee, S.Y.; Kim, J.M.; Ahn, J.H.; Kim, P.; Choi, J.Y.; Hong, B.H.; *Nature*, **2009**, *457*, 706. **DOI:** 10.1038/nature07719
11. Shokry, S.A.; El Morsi, A.K.; Sabaa, M.S.; Mohamed, R.R.; El Sorogy, H.E.; *Egypt J Pet*, **2014**, *23*, 189. **DOI:** 10.1016/j.ejpe.2014.05.005
12. Charisiou, N.D., Baklavaridis, A.; Papadakis, V.G.; Goula, M.A.; *Waste Biomass Valori*, **2016**, *7*, 725. **DOI:** 10.1007/s12649-016-9627-9
13. Charisiou, N.D.; Siakavelas, G.; Papageridis, K.N.; Baklavaridis, A.; Tzounis, L.; Avraam, D.G.; Goula, M.A.; *J Nat Gas Sci Eng*, **2016**, *31*, 164. **DOI:** 10.1016/j.jngse.2016.02.021
14. Goula, M.A.; Charisiou, N.D.; Papageridis, K.N.; Delimitis, A.; Pachatouridou, E.; Iliopoulou, E.F.; *Int J Hydrogen Energy*, **2015**, *40*, 9183. **DOI:** 10.1016/j.ijhydene.2015.05.129
15. Bereketidou, O.A.; Goula, M.A.; *Catal Today*, **2012**, *195*, 93.
16. Yentekakis, I.V.; Goula, G.; Panagiotopoulou, P.; Katsoni, A.; Diamadopoulos, E.; Matzavinos, D.; Delimitis, A.; *Top Catal*, **2015**, *58*, 1228. **DOI:** 10.1007/s11244-015-0490-x
17. Usman, M.; Wan Daud, W.M.A.; Abbas, H.F.; *Renew Sustainable Energy Rev*, **2015**, *45*, 710. **DOI:** 10.1016/j.rser.2015.02.026
18. Avraam, D.G.; Halkides, T.I.; Liguras, D.K.; Bereketidou, O.A.; Goula, M.A.; *Int J Hydrogen Energy*, **2010**, *35*, 9818. **DOI:** 10.1016/j.ijhydene.2010.05.106
19. Charisiou, N.D.; Iordanidis, A.; Polychronopoulou, K.; Yentekakis, I.V.; Goula, M.A.; *Mater Today Proce*, **2017** – Accepted for publication
20. Gurav, H.R.; Dama, S.; Samuel, V.; Chilukuri, S.; *J CO2 Util*, **2017**, *20*, 357. **DOI:** 10.1016/j.jcou.2017.06.014
21. Titus, J.; Roussiere, T.; Wasserschaff, G.; Schunk, S.; Milanov, A.; Schwab, E.; Wagner, G.; Oeckler, O.; Glaser, R.; Catal Today, **2016**, 270, 68. **DOI:** 10.1016/j.cattod.2015.09.027
22. Serrano-Lotina, A.; Daza, L.; *J Power Sources*, **2013**, *238*, 81. **DOI:** 10.1016/j.jpowsour.2013.03.067
23. Goula, M.A.; Charisiou, N.D.; Siakavelas, G.; Tzounis, L.; Tsiaoussis, I.; Panagiotopoulou, P.; Goula, G.; Yentekakis, I.V. *Int J Hydrogen Energy*, 2017, 42, 13724. **DOI:** 10.1016/j.ijhydene.2016.11.196
24. Papageridis, K.N.; Charisiou, N.D.; Siakavelas, G.; Avraam, D.G.; Tzounis, L.; Kousi, K.; Goula, M.A.; *Fuel Process Technol*, **2016**, *152*, 156. **DOI:** 10.1016/j.fuproc.2016.06.024
25. Si, R; Zhang, Y.W.; Li, S.G.; Lin, B.X.; Yan, C.H.; *J. Phys. Chem. **B 2004**, 108, 12481* **DOI:** 10.1021/jp048084b
26. Nikoo, M.K.; Amin, N.A.S.; *Fuel Process Technol*, **2011**, *92*, 678. **DOI:** 10.1016/jfuproc.2010.11.027
27. Lehman, J.H.; Terrones, M.; Mansfield, E.; Hurst, K.E.; Meunier, V.; *Carbon*, **2011**, *49*, 1581 **DOI:** 10.1016/jcarbon.2011.03.028
28. Tzounis, L.; Kirsten, M.; Simon, F.; Mader, E.; Stamm, M.; *Carbon*, **201**, *73*, 310. 112. **DOI:** 10.1016/j.carbon.2014.02.069
29. Tsirka, K.; Foteinidis, G.; Dimos, K.; Tzounis, L.; Gournis, D.; Paipetis, A.S.; *J Colloid Interface Sci*, **2017**, *487*, 444. **DOI:** 10.1016/j.jcis.2016.10.075
30. Liu, J.; Wang, C.; Tu, X.; Liu, B.; Chen, L.; Zheng, M.; Zhou, C.; *Nat Commun*, **2012**, *3*, 1199. **DOI:** 10.1038/ncomms 2205
31. Tsiaoussis, I. et al., Book of Abstracts, Session W2 Nanoparticles, 14th International Conference of Nanosciences & Nanotechnologies, **2017**.
32. Si, R.; Zhang, Y.W.; Li, S.J; Lin, B.X.; Yan, C.H.; *J. Phys. Chem. B **2004**, 108, 12481*. **DOI:** 10.1021/jp.048084b

Supporting information

a) Experimental setups

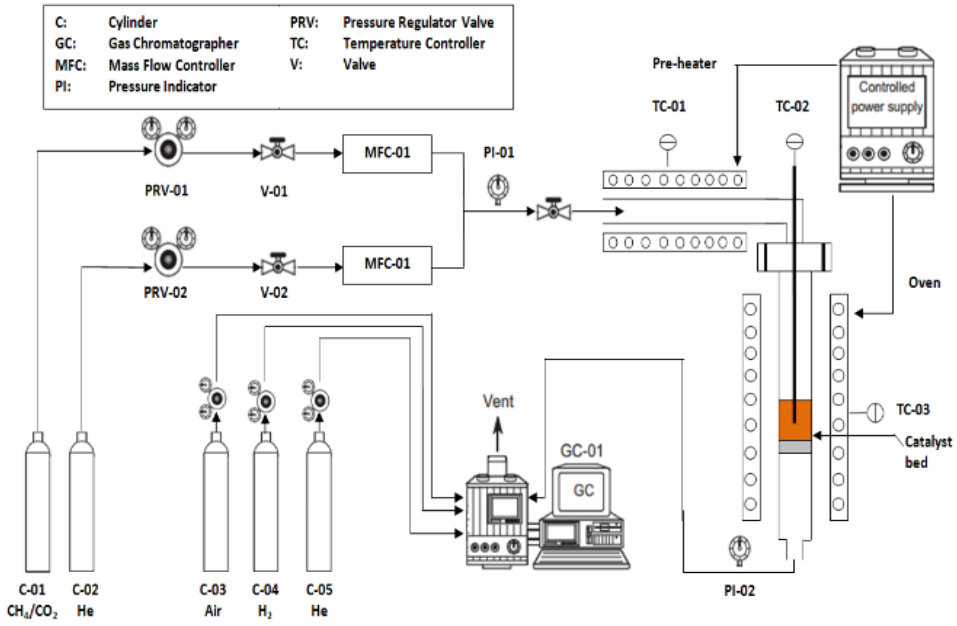

Fig.1. Schematic flow chart of experimental setup for activity test of catalysts for the biogas dry reforming.

b) Methods

HAADF-STEM, ABF imaging and high-resolution EDX-STEM. HAADF-STEM, ABF-STEM and EDX-STEM experiments were acquired using a Jeol 2100 FEG microscope equipped with a Bruker EDX detector operated at 200 kV. The results were recorded using probes with convergence semi-angles in the 21–25 mrad range (with a probe size of about 2nm). The probe current ranged between 50 and 200 pA.